Bo Zhao · Haiquan Zhang · Liao Hongjian · Weile Li · Lijun Su · Wenxiu He · Lu Zeng · Haokun Qin · Megh Raj Dhital

Emergency response to the reactivated Aniangzhai landslide resulting from a rainstorm-triggered debris flow, Sichuan Province, China

Abstract On June 17, 2020, an unexpected rainstorm struck the Meilong valley, which is located in Danba County, Sichuan Province, China. The cumulative rainfall of this short-duration event reached 38.1–42.4 mm and triggered the Meilong debris flow. The Meilong debris flow rushed into the valley and forced the Xiaojinchuan (XJC) River to flow along the foot of the ancient Aniangzhai (ANZ) landslide. Intense erosion reactivated the ancient ANZ landslide, producing a reactivated area of 0.62 km². Subsequently, emergency investigation and monitoring were conducted to monitor its deformation because unstable landslide conditions could pose a serious threat to the safety of lives and property downstream. Emergency monitoring over 20 days (June 23, 2020–July 12, 2020) indicated that the reactivated deposit decelerated and entered the constant deformation state; careful attention should be paid to this reactivated deposit.

Keywords Reactivated Aniangzhai landslide · Rainstorm · Debris flow · Emergency monitoring

Introduction

Landslides are common natural hazards all over the world and can result in considerable loss of life and damage to infrastructure, and reactivated landslides are especially common (Hewitt 1988, Keefer 1994, Korup et al. 2007, Huang 2009, Paronuzzi and Bolla 2012, Su et al. 2017, Wang et al. 2018, Zhao et al. 2019, Li et al. 2020). A reactivated landslide refers to an existing landslide deposit that becomes active again in response to one or more triggers, such as rainfall, earthquakes, reservoir impoundment, engineering construction, and others, which alter the stress balance (Prior et al. 1989, Flageollet et al. 1999, Borgatti et al. 2006, Matsuura et al. 2008, Wang et al. 2008, Lin et al. 2011, Massey et al. 2013, Burda et al. 2013, Bozzano et al., 2013, Barla et al. 2015, Dixon et al. 2015, Luo et al. 2017, Gu et al. 2017, Song et al. 2018, Li et al. 2020). It is of great importance to clarify the movement features of reactivated landslides, determine the potential triggers, and predict whether a landslide will fail catastrophically and produce hazardous consequences (Gu et al. 2017, Li et al. 2020).

To promote the study of deformation features of reactivated landslides, we report a recent landslide case, namely, the Aniangzhai (ANZ) landslide, which was reactivated by the intense erosion of a new river channel in Sichuan Province, China. After the landslide was reactivated, emergency field investigations and emergency monitoring were carried out to detect its deformation characteristics and failure mechanism to provide guidance for further management.

Study area and emergency response scheme

Study area

The reactivated ANZ landslide (102° 1′ 37.31″ E, 30° 58′ 38.92″ N) is located in Banshanmen town, Danba County, Sichuan Province,

China (Figs. 1 and 2), which lies in the west-central section of Sichuan Province and is part of the transition zone between the Qinghai–Tibetan Plateau and the Sichuan Basin (Fig. 1(B)). The transition zone is a famous area of active tectonics, and numerous geohazards are concentrated in this zone (Zhao 2020). The landslide site is also located close to the interaction of the Longmenshan fault zone and the Xianshuihe fault zone (Fig. 1(B)). These two fault zones are very active, and many earthquakes have occurred along them, such as the 1786 Moxi Ms 7.75 earthquake (Xianshuihe fault zone) and the 2008 Wenchuan Ms 8.0 earthquake (Longmenshan fault zone) (Dai et al. 2005, Xu et al. 2009).

The landslide site has a monsoon climate, and the annual average temperature is approximately 14.6 °C. The annual rainfall is approximately 532.7–823.3 mm and is mainly concentrated in May–September, accounting for more than 80.2% of the annual rainfall (based on data provided by the Danba Meteorological Bureau). The strata near the event site mainly consist of quartzite and phyllite belonging to the Devonian Weiguan Group (CIGMR 1985a, 1985b). The landslide site mainly contains 3 features of (1) the XJC River (Fig. 1(C)), (2) the Meilong valley (Fig. 2(A)), and (3) the ancient ANZ landslide (Fig. 2(C and D)).

1. XJC River. The landslide is located along the downstream stretch of the XJC River, which is a branch of the Dadu River (Fig. 1(C)). The XJC River originates from the Qionglai Mountains and has a length, natural fall, and basin area of 151 km, 2340 m, and 5323 km², respectively (Li 2012). Topographically, the river flows mainly through deeply cut gorges (Bai et al. 2020). A power station (Guanzhou station) is located near the event site, and two local weather stations are located in Banshanmen town and Anianggouer village (Fig. 2(A)).

2. Meilong valley. The Meilong valley, which ranges from 2119 to 4439 m in elevation, lies on the right bank of the XJC River and covers an area of 62.55 km². The length of the main gully is approximately 10 km (Fig. 2(B)). The average longitudinal gradients of the whole section and of the entrance section of the main gulley are approximately 0.157 and 0.108 (Fig. 2(B)), respectively, and the slopes in the valley area are usually steeper than 40°. The Meilong valley is a low-frequency debris flow valley according to locals. Numerous trees and villages were present in the gully bottom.

3. Ancient ANZ landslide. The ancient ANZ landslide is located on the left bank of the XJC River, and its upstream foot is located at the entrance of the Meilong valley (Fig. 2(A)). The ANZ landslide is a giant ancient landslide that once blocked the XJC River. According to local residents, the
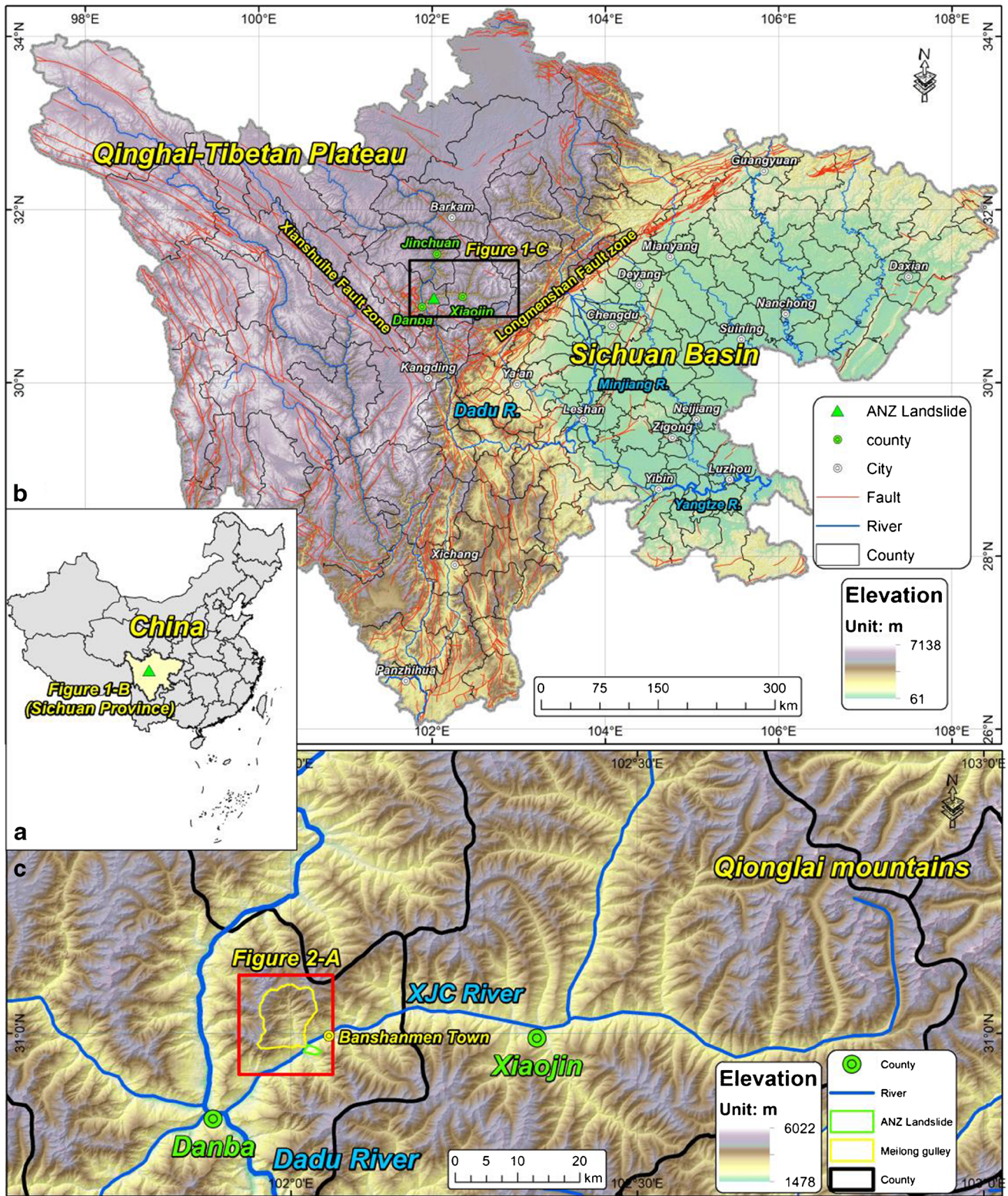
Fig. 1 Regional setting and location of the study area. (**A**) Study area map. (**B**) Landslide location in Sichuan Province and regional setting. (**C**) Spatial relationship of ANZ landslide and XJC River. The fault data are from Zhao et al. (2019)

ancient ANZ landslide experienced very slow creep deformation in recent years, as evidenced by the occasional cracking of many buildings and farmland on the deposit. The pre-event satellite image also shows some local scarps
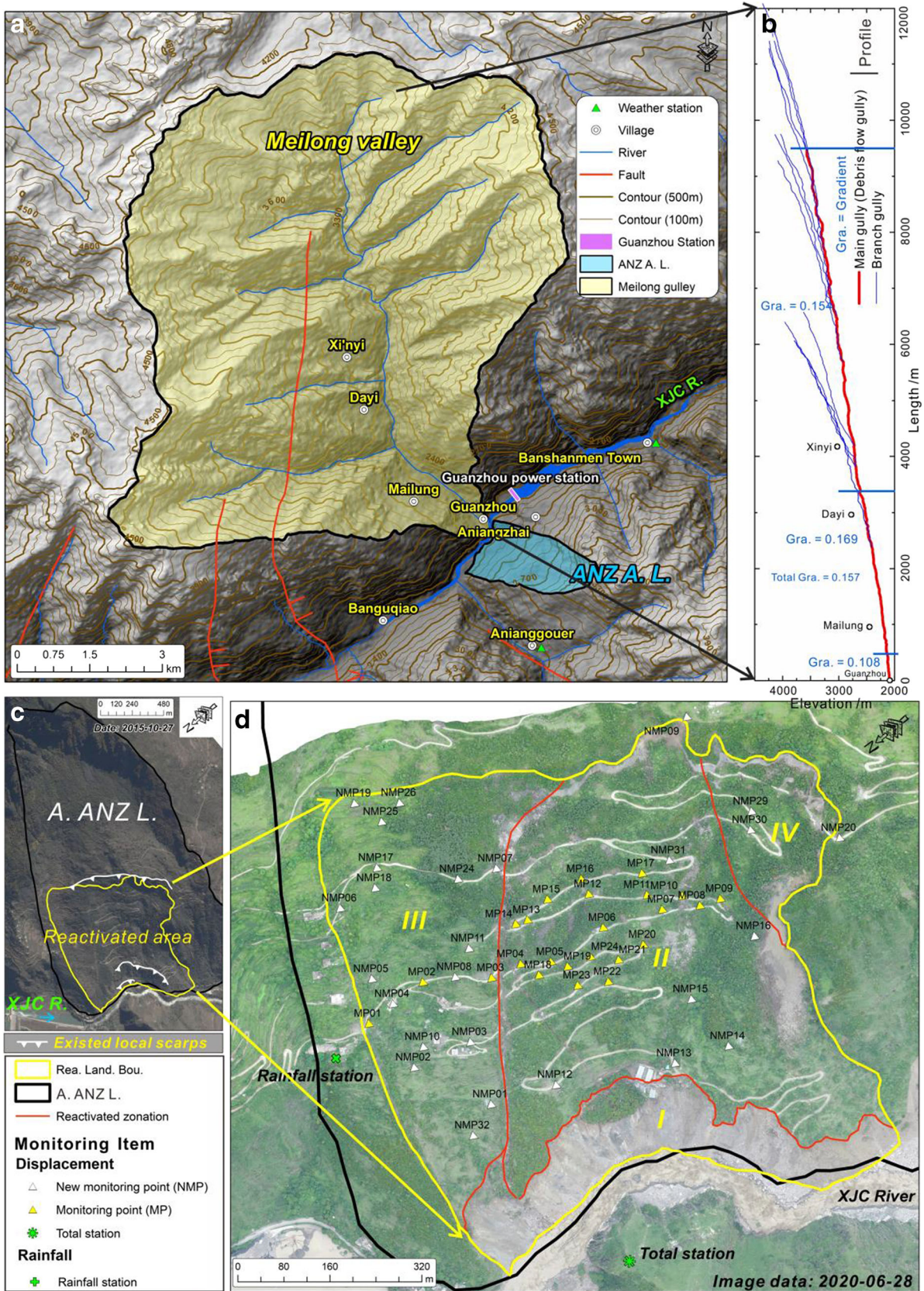
Fig. 2 Detailed characteristics of the Meilong valley and ancient ANZ landslide. (**A**) Topographic features and fault distribution. (**B**) Profiles of Meilong valley. (**C**) Overall characteristics of the ancient ANZ landslide. (**D**) The detailed characteristics of the reactivated ANZ area and emergency monitoring scheme. XJC R., Xiaojinchuan River; A. ANZ L., ancient Aniangzhai landslide, Rea. Land. Bou., reactivated landslide boundary; the fault in (A) is from CIGMR (1985a, 1985b), (C) is from Google Earth. I–IV in (D) is landslide deformation zonation
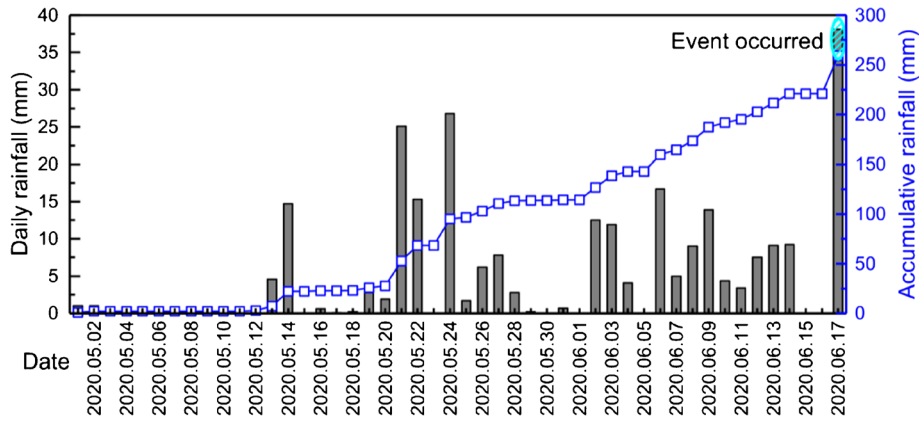
Fig. 3 Daily rainfall distribution before the Danba event according to the Anianggouer station. The daily rainfall data are from the Danba Meteorological Bureau, and the location of the Anianggouer station is shown in Fig. 2(A)

in the front deposit area (Fig. 2(B)), which indicates that some deposit failures had occurred.

Data preparation

To detect the deformation characteristics and potential failure mechanism of the reactivated ANZ landslide, several emergency investigations and monitoring were carried out (Fig. 2(D)), and regional data, such as geological maps, digital elevation models (DEMs) (12.5 m), and satellite images, were also collected.

For emergency investigation and monitoring, an unmanned aerial vehicle (UAV) was used to obtain field images (June 18, 2020) only 1 day after the catastrophic debris flow, and an emergency field investigation was also performed, which found that the ancient ANZ landslide was reactivated. The emergency monitoring team entered the site on June 23, 2020, and the daily UAV and total station monitoring scheme began (Fig. 2(D)). Fifty-six monitoring points covering the whole reactivated deposit area were evaluated

to detect the deformation scale and direction; their distribution and other detailed information are given in Fig. 2(D). For this study, the UAV images and monitoring data were accessed up to July 12, 2020. Because it was too dangerous to establish monitoring points in the reactivated front area (zone I), 3 monitoring points (NMP12, NMP13, and NMP14) were set up as close as possible to the front area (zone I) to capture its deformation features (Fig. 2(D)). In addition, one rainfall monitoring station was established to analyze the relationship between rainfall and the deformation rate (Fig. 2(D)), and daily flow data for the XJC River were also collected from the Guanzhou power station.

The UAV was a DJI Phantom 4 real-time kinematic (RTK) instrument, which is a high-precision aerial survey UAV (https://www.dji.com/cn/phantom-4-rtk). To ensure the comparability of the UAV images, we maintained the same air route, launch point (near the location of the total station), relative altitude (480 m higher than the launch point), and image overlap ratio (70%). The UAV images with coordinate
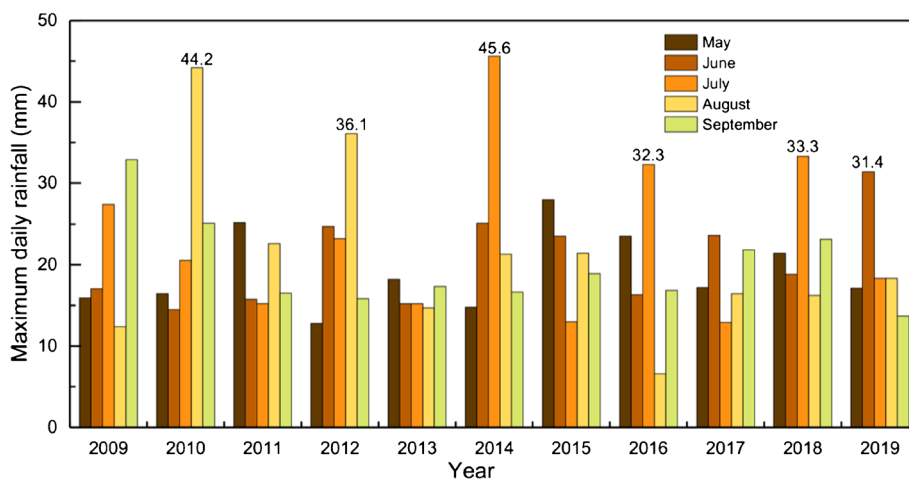

Fig. 4 The distribution of maximum daily rainfall between May and September from 2009 to 2019 according to the Anianggouer station (unit: mm; the data are from the Danba Meteorological Bureau)
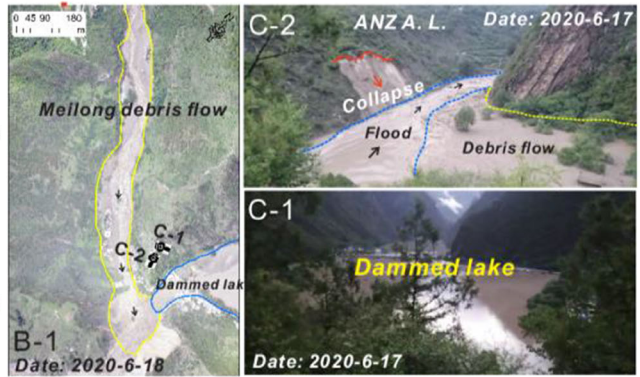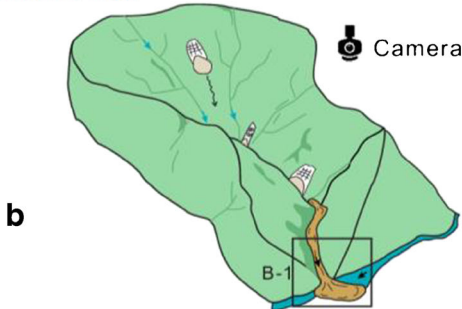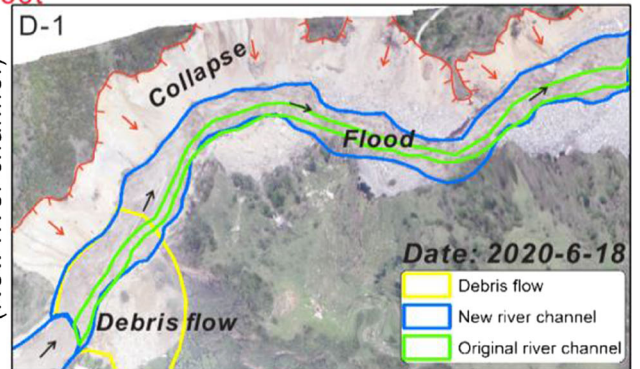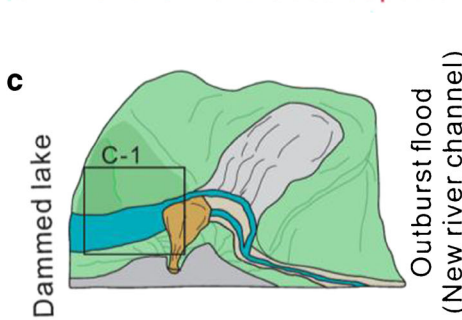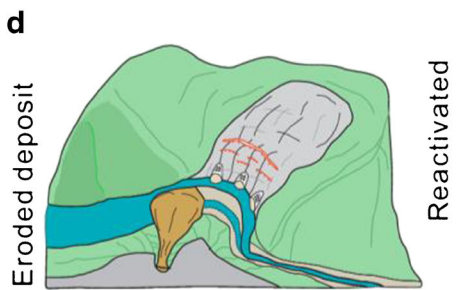
Fig. 5 The evolution process of the reactivated ANZ landslide. (**A–D**) Sketches of the evolution process along with field and UAV images. (**A**) The unexpected rainstorm; (**B, B-1**) the typical characteristics of the Meilong debris flow; (**C, C-1 and C-2**) the dammed lake and the new river channel; (**D, D-1 and D-2**) the front collapses of the ancient ANZ landslide (**D-1**) and the overall area of reactivated landslide (**D, D-2**). The photos in (**C-1**) and (**C-2**) were taken on June 17, 2020 by local residents

information were imported into the Smart3D software to obtain orthographic images of the reactivated landslide, and the orthographic image resolution was approximately 0.13 m.

Intense erosion reactivated the Aniangzhai landslide

According to descriptions by local residents (Guanzhou village in Fig. 2(A)), on the night of June 16th, 2020, a rainstorm struck the Meilong valley. The nearby Banshanmen and Anianggouer

weather stations (locations are listed in Fig. 2(A)) indicated that the cumulative rainfall during this period reached 38.1 mm and 42.4 mm, respectively. Figure 3 shows the daily rainfall from May 1th, 2020, to June 17th, 2020, (48 days) before the ANZ event. Figure 3 indicates the daily rainfall amounts before the ANZ event (June 16th) were mainly less than 30 mm. Figure 4 shows the maximum daily rainfall between May and September (rainy season) in the last 10 years near landslide site. Figure 5 reveals that, in
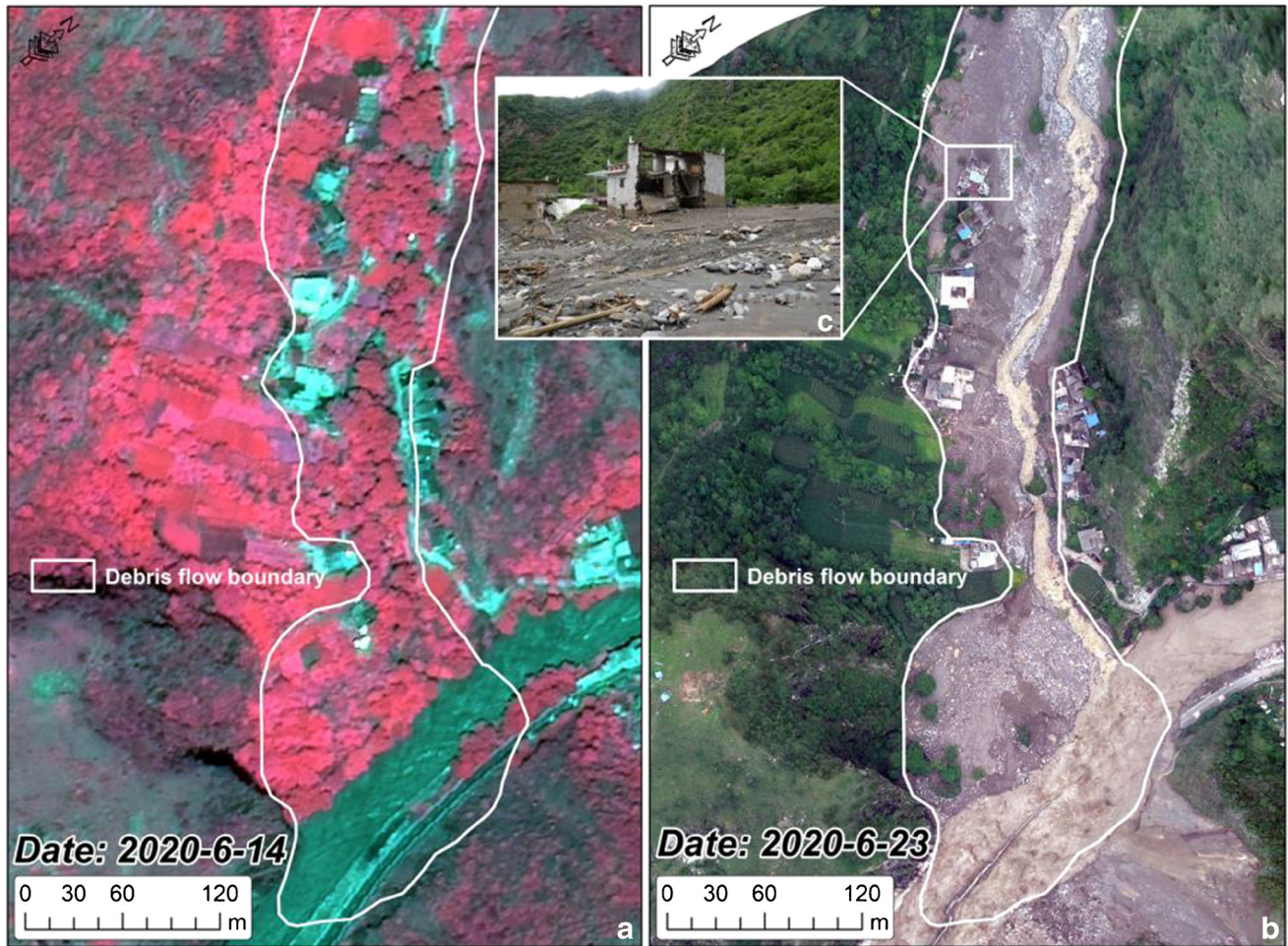
Fig. 6 Typical characteristics of the Meilong debris flow. (**A** and **B**) Images before (satellite image) and after (UAV image) the Meilong debris flow. (**C**) Buildings were damaged by debris flow
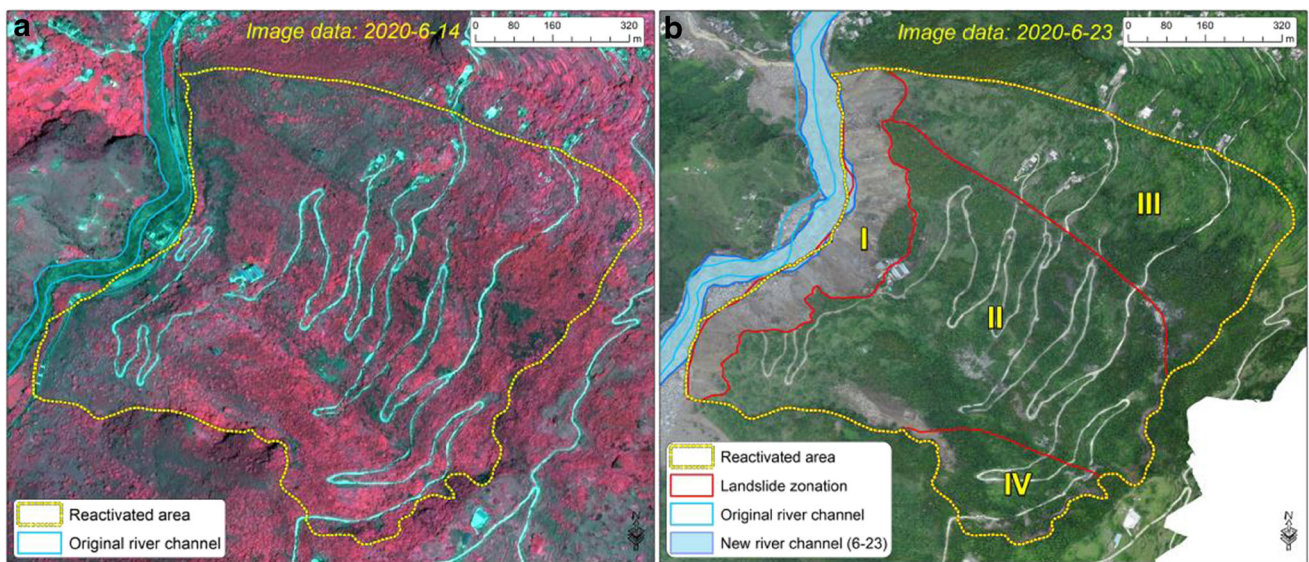

Fig. 7 Images of the ancient ANZ landslide before and after the Meilong debris flow indicate that the ancient ANZ landslide was reactivated. **a** Satellite image before the Meilong debris flow. **b** UAV image after the Meilong debris flow. The satellite image is from Gaofen-2
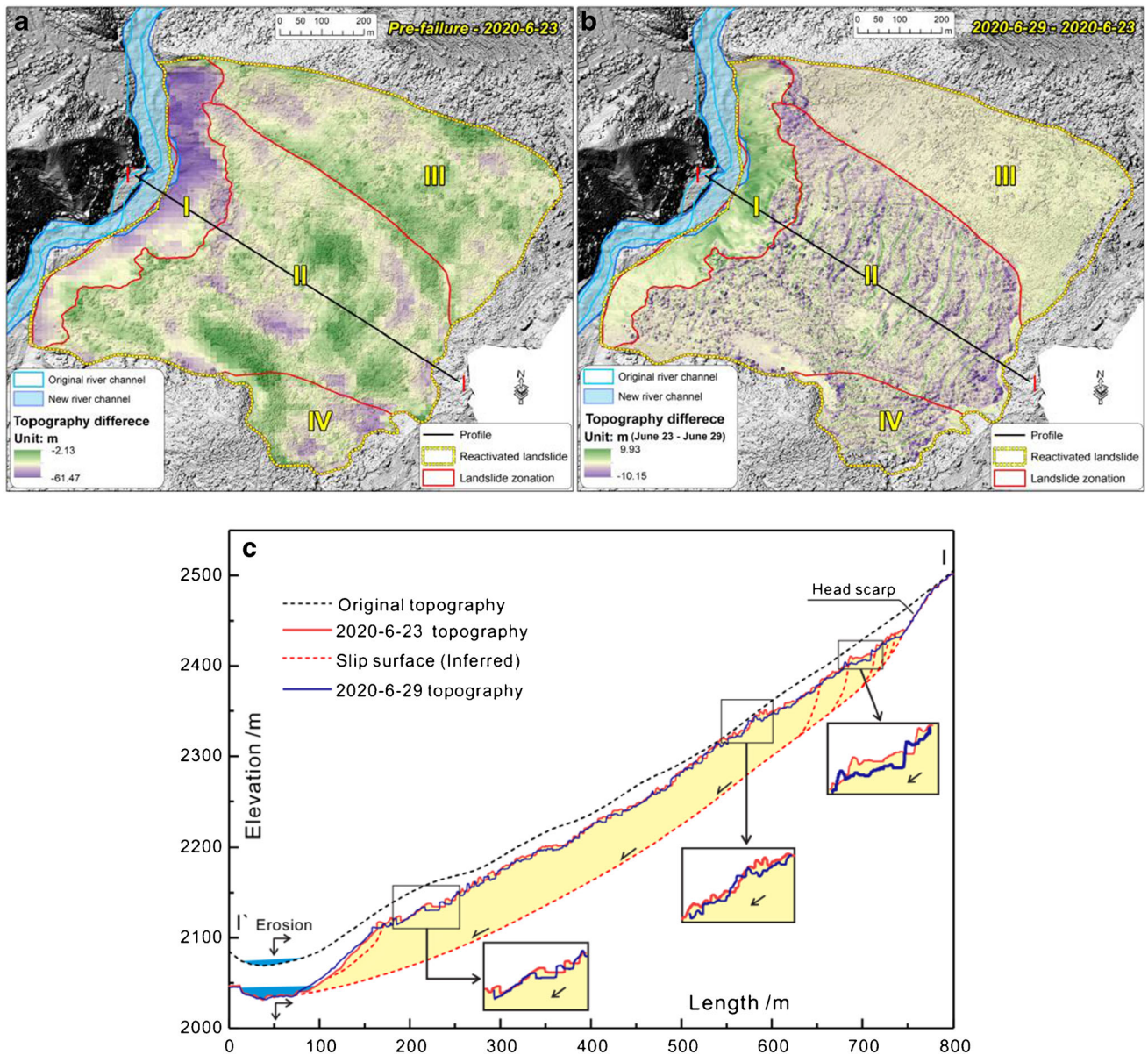
Fig. 8 The topographic variations between different periods. **a** The topographic difference between the June 29, 2020 topography and the original topography. **b** The topographic difference between June 29, 2020 and June 23, 2020. **c** The profile variations of different periods. The slip surface was inferred from microtopography variation, outcrops of existed slipping surface and potential surface rupture

these years, the maximum daily rainfall during May–June was mainly concentrated within 15–28 mm (Fig. 5). From above, this short, intense rainstorm near ANZ event date exceeded the maximum daily rainfall of the past 10 years.

The short, intense rainstorm (Fig. 5(A)) activated the deposits accumulated in the gully (Fig. 5(B)). At approximately 3:00 am on June 17, the Meilong debris flow occurred. The debris flow lasted approximately 3–4 h. The debris flow rushed out of the Meilong valley into the XJC River and partially blocked the river (Fig. 5(B-1)), and a dammed lake was formed (Fig. 5(C and C-1)). The images pre- and post-Meilong debris flow indicate that the deposits covered the whole gully bottom, with widths ranging from 20 to 80 m, and that some buildings were damaged (Fig. 6). The depth and volume of the Meilong debris flow were 6–12 m and 0.4 Mm³, respectively, according to field investigations.

According to local residents, a person in Guanzhou village received a call from someone in Dayi village at 3:03 am about the occurrence of the debris flow at Dayi village. Then, at approximately 3:09 am, the resident in Guanzhou village saw the debris flow (the locations of two villages are shown in Fig. 2(A)). The distance between Dayi village and Guanzhou village is approximately 3 km, which indicates that the debris flow velocity between these two villages was approximately 0.5 km/min (8.3 m/s).

The fast-moving debris flow rushed into the XJC River (Fig. 5(C and C-2)), raised the riverbed by approximately 8–12 m, and formed a dammed lake (Fig. 5(C-1)). On the morning of June 17, the river overflowed the front section of the deposit and formed a new river channel (Fig. 5(C-2)), and this new channel lay at the foot of the ancient ANZ landslide (Fig. 5(D and D-1)). The new river channel intensely eroded the foot of the ancient ANZ landslide, and some collapses occurred on the morning of June 17th (Fig. 5(C-2)). On June 18, the whole front collapsed (Fig. 5(D-1)), and the ancient ANZ landslide was reactivated (Fig. 5(D and D-2)). The images of ancient ANZ landslide before and after the Meilong debris flow indicate that obvious deformation began to appear throughout the reactivated area covering an area of 0.62 km² (Fig. 7).

Emergency response to the reactivated Aniangzhai landslide

Basic deformation characteristics of the reactivated Aniangzhai landslide

To detect the basic deformation of the reactivated area, two topographic difference maps before and after reactivation and in different periods after reactivation are depicted (Fig. 8a, b), and the profile variations of different periods were also obtained (Fig. 8c). From the topographic difference map before and after reactivation (Fig. 8a), the whole reactivated area underwent obvious deformation, especially in the front section where maximum elevation change reached approximately 61.5 m.

From the topographic difference of different periods after reactivation (June 23, 2020–June 29, 2020), topographic growth appears in the front section, while topographic reduction mainly
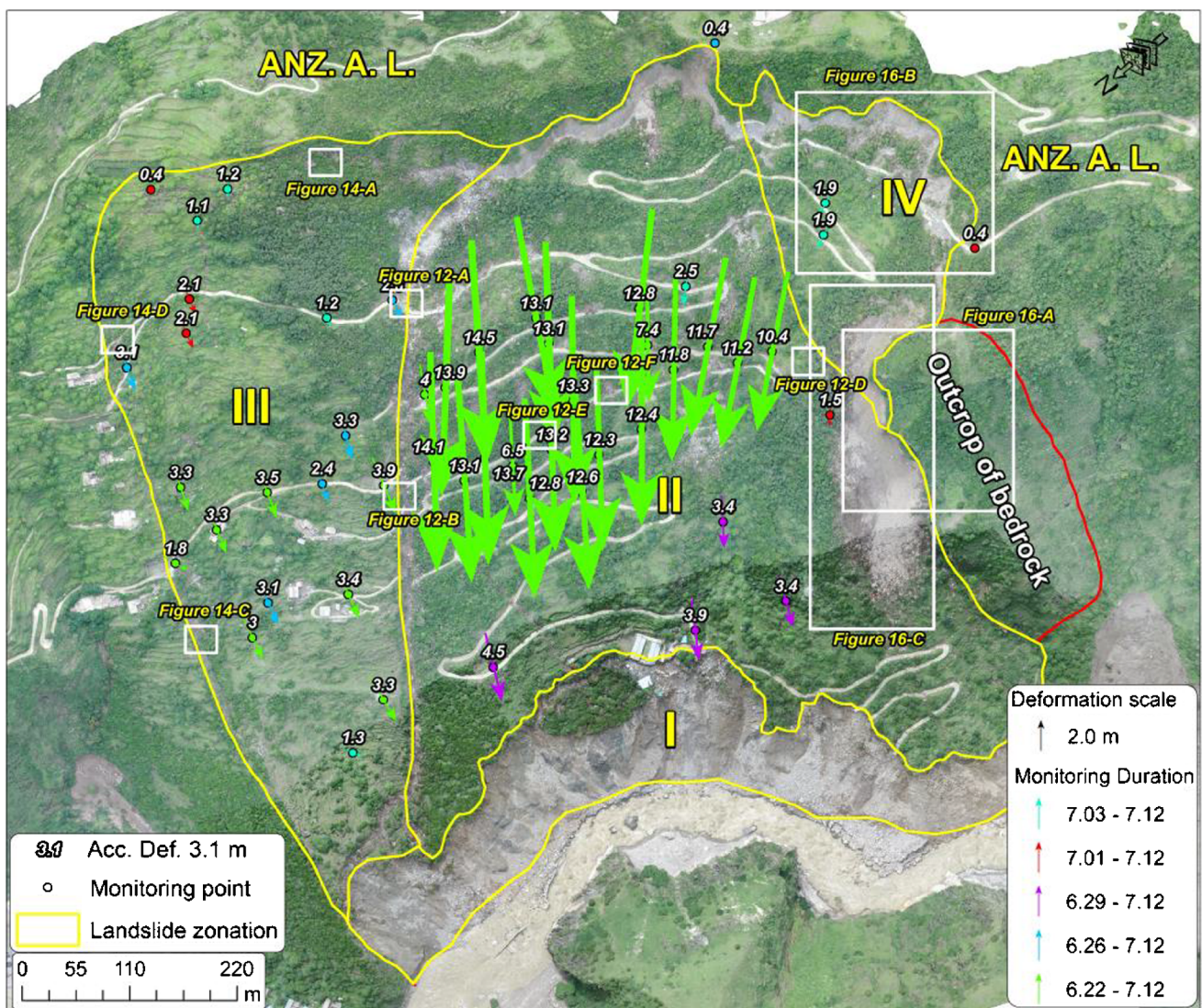

Fig. 9 The deformation vector distribution of reactivated deposits according to the emergency monitoring scheme. Acc. Def., accumulative deformation. The locations of the monitoring points are listed in Fig. 2(D)

appears in the middle and rear sections (Fig. 8b). The reactivated landslide slipped downward as a whole because the movement did not change the microtopography but, rather, the relative positions of the points (Fig. 8c).

Figure 9 shows the distribution of deformation vectors of monitoring points. From Fig. 9, the middle section of the reactivated part is approximately perpendicular to the river channel, which is the normal direction. The deformation scales of middle section were the largest. The movement directions of the two lateral sections are mainly related to that of the middle section, especially the downstream section (Fig. 9).

According to basic deformation characteristics and corresponding scales of deposits in the reactivated area and the locations of lateral flanks, the reactivated area can be divided into 4 subzones: zone I—front collapse zone; zone II—main
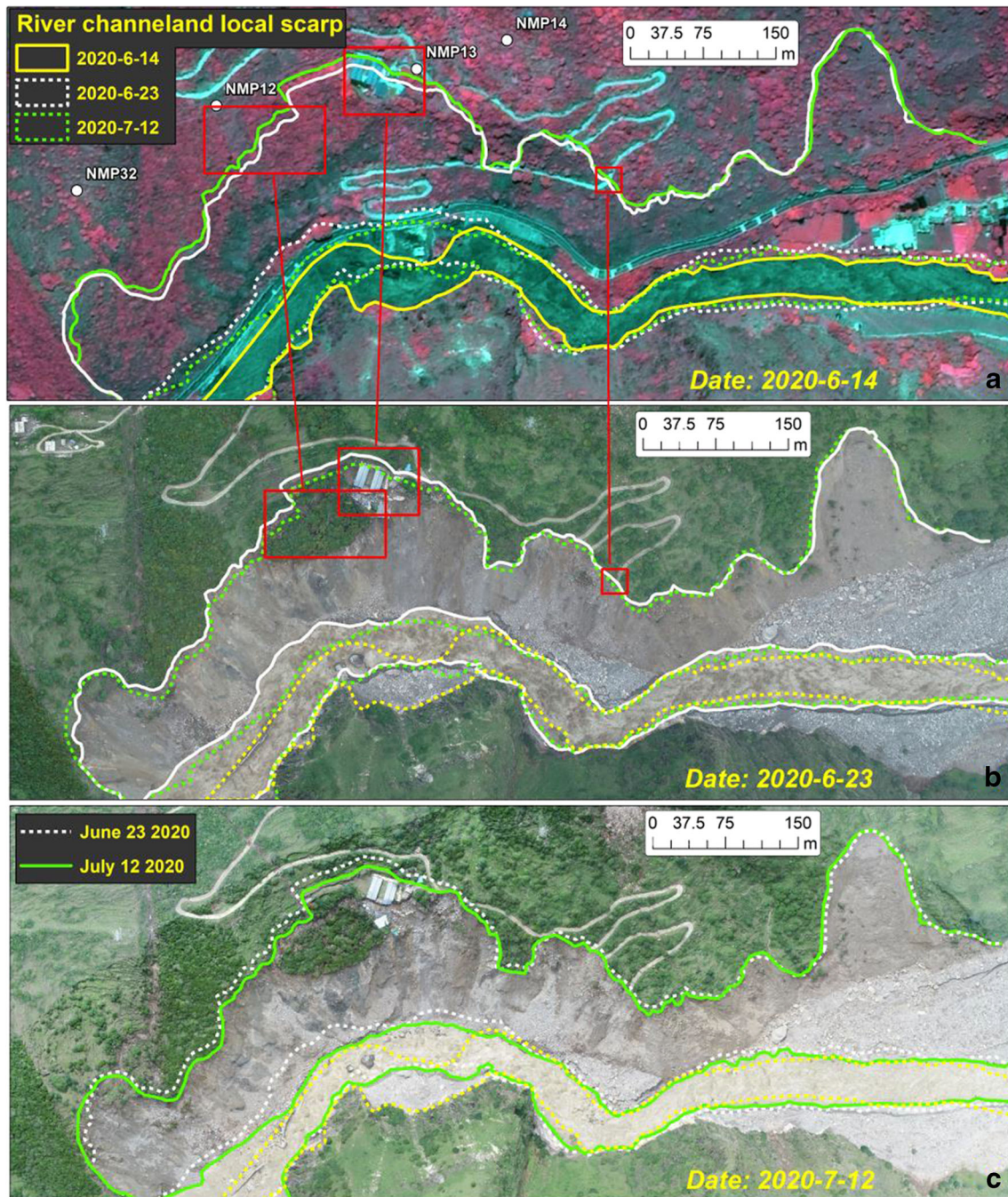

Fig. 10 The different periods of satellite (**A**) and UAV (**B** and **C**) images show the collapse characteristics of the front collapse zone (I). Image A is from Gaofen-2; the red boxes in (**A**) and (**B**) show the obvious deformation that occurred in these places

deformation zone; zone III—upstream deformation zone; and zone IV—downstream deformation zone, as shown in Figs. 8 and 9. The following sections will discuss the detailed deformation characteristics of the different reactivated zones.

Detailed deformation characteristics

Front collapse zone I

Front collapse zone I is located in the front section of the reactivated area and covers an area of 4.68×10^4 m² (Figs. 9 and 10). The satellite and UAV images indicate that the new river channel flows along the foot of reactivated deposit and the current river is slightly wider than pre-event channel (Fig. 10). The UAV image from June 23 indicates all collapses appeared in this zone (Fig. 10(B)). The UAV images from June 23 to July 12 indicate no further obvious collapses occurred in this zone, but the overall movement was forward, with displacements reaching 6–11 m (Fig. 10). The intense erosion caused a mass loss of more than 2.8 Mm³ in zone I according to the calculation of topographic difference.

Figure 11 shows the deformation rate of monitoring points in zone I. All monitoring points present similar distribution patterns in a similar direction despite some differences in values (Figs. 9 and 11). The initial deformation rates in the horizontal direction and vertical direction reached 20–40 mm/h and 10–20 mm/h, respectively (Fig. 11), and the cumulative deformation increased rapidly. Then, the deformation rate decreased slowly. By July 12, 2020, the deformation rates in the two directions were both less than 5 mm/h (Fig. 11).

Main deformation zone II

The main deformation zone II is located in the middle of the reactivated area covering an area of 2.99×10^5 m² (Fig. 9), and this is the largest subzone, occupying 49% of the total reactivated area.

Zone II is the area with the most intense deformation, and obvious local head scarps and lateral flanks are present (Figs. 9 and 12).

The roads were destroyed at the boundary of zone II and zone III, where the vertical dislocation reached 5–14 m (Fig. 12(A and B)). Slickensides are obvious on the lateral flanks (Fig. 12(C)). A similar phenomenon also appears in the local head scarp area (Fig. 12(O)), and the dislocations of the local head scarps reach 15–20 m in the horizontal direction and 15–25 m in the vertical direction. Numerous fissures have formed near the downstream boundary (Fig. 12(D)).

The deformation directions in both zone III and IV can be decomposed with a deformation component toward zone II (Fig. 9). Therefore, the zone II features superimposed latitudinal compression, producing some instances of road uplift (parallel to the deformation direction) in zone II (Fig. 12(E)). Numerous surficial collapses are also concentrated in this zone (Fig. 12(F)).

Figure 13 shows the deformation rate of monitoring points in zone II. Similar to the distribution patterns of the monitoring points in zone I, all monitoring points present similar distributions in the same direction despite some differences in values (Figs. 9, 11, and 13). The initial deformation rates in the horizontal direction and vertical direction reached 50–200 mm/h and 20–120 mm/h, respectively (Fig. 13), and the cumulative deformation increased rapidly. With time, the deformation rate decreased obviously; by July 12th, 2020, the deformation rates in the two directions were both approximately 5 mm/h (Fig. 13). The cumulative deformation values were also stable and reached 10.4–14.5 m in the horizontal direction and 7.1–11.4 m in the vertical direction.

Upstream deformation zone III

Upstream deformation zone III is located in the upstream section and covers an area of 1.86×10^5 m² (Fig. 9), making it the second largest subzone, occupying 30% of the total reactivated area. Compared with zone II, this zone shows no obvious deformation
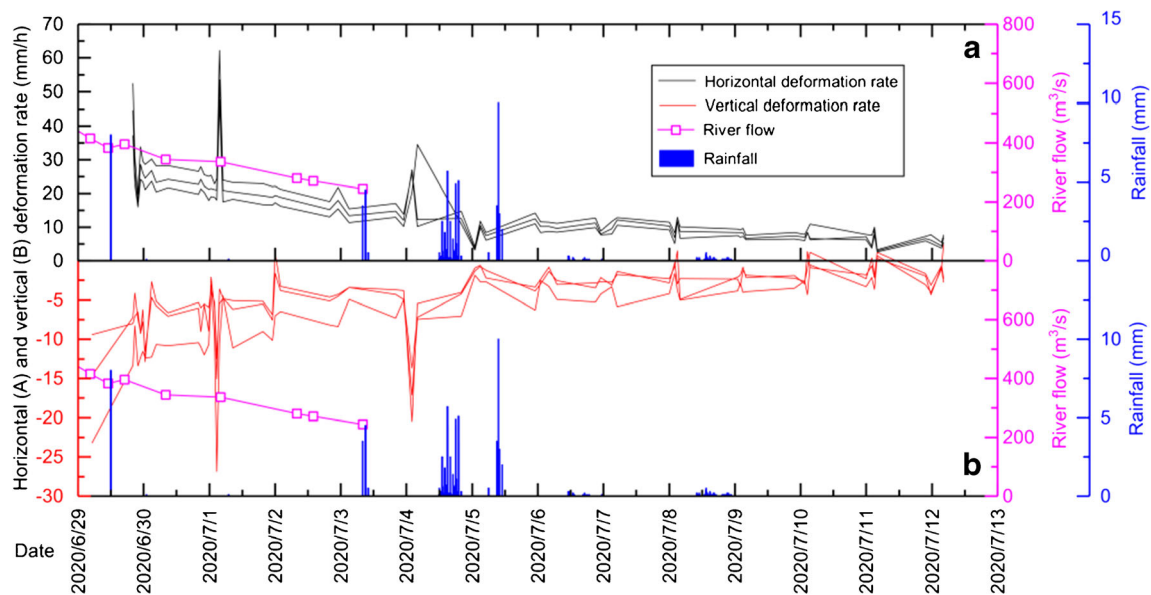

Fig. 11 The deformation rate of monitoring points in front collapse zone I. (**A**) Horizontal deformation rate. (**B**) Vertical deformation rate. The rainfall data is from self-built rainfall station whose location is listed in Fig. 2(D), the river flow data is from Guanzhou power station whose location is listed in Fig. 2(A). The rainfall data and river flow data in Figs. 13, 15, and 17 are the same with Fig. 11

phenomena in terms of topographic differences (Fig. 8), while the field investigations indicate that multistage local head scarps with dislocations ranging from 0.5 to 2.2 m formed (Fig. 14a and b). The upstream boundary mainly consists of fissures with widths less than 15 cm (Fig. 14c), and some roads were damaged (Fig. 14d). The characteristics of the downstream boundary can be found in Fig. 12(A and B). The shape of this zone is an inverted trapezoid, and increasingly narrow deformation space caused the deposits in zone III to expand in the latitudinal direction. Therefore, zone III presents a composite deformation direction oriented downward toward zone II.

Figure 15 shows the deformation rate of monitoring points in zone III. All monitoring points present similar distribution patterns in the same direction despite some differences in values (Figs. 9 and 15). However, unlike the distribution patterns in zones I and II, the pattern in this zone shows a deformation rate that first

increased and then decreased very slowly, and the current deformation rate is approximately 5 mm/h (Fig. 15). The cumulative displacement of zone III presented an approximately uniform increase and reached approximately 3.0 m in the horizontal direction and approximately 1.7 m in the vertical direction. From Figs. 11, 13, and 15, the fluctuations of rainfall and river flow have no obvious influences on the deformation rate of reactivated deposits.

Downstream deformation zone IV

Downstream deformation zone IV is located in the downstream and upper sections of the reactivated area and covers an area of 4.68×10^4 m² (Fig. 9). Because of the obstruction by a bedrock outcrop in the sliding direction (Figs. 9 and 16(A)), the sliding direction was deflected toward zone II. The dislocation of head scarp ranged from 20 to 30 m in the horizontal direction and 15–25 m in the vertical

Fig. 12 Typical characteristics of main deformation zone II. (O) obvious dislocation in the local scarp area, (A and B) dislocation of a road and a lateral flank at the upstream boundary, (C) slickensides on the upstream flank, (D) numerous fissures at the downstream boundary, (E) uplift of a road in the middle section of zone II, and (F) a surficial collapse in zone II. The locations of (A), (B), (D), (E), and (F) are listed in Fig. 9
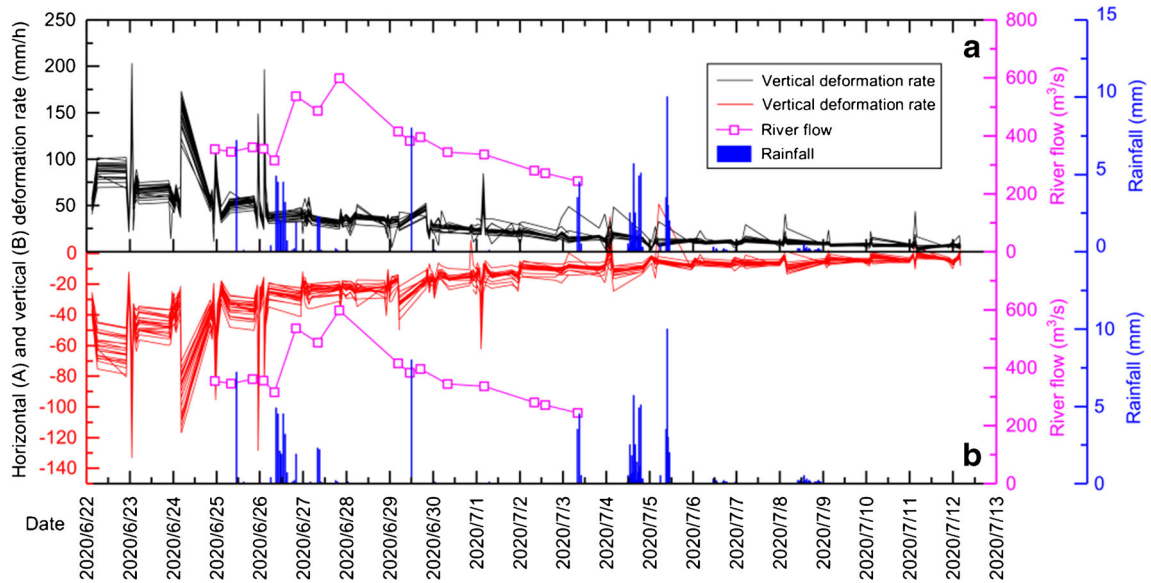
Fig. 13 The deformation rates of monitoring points in main deformation zone ll. (**A**) Horizontal deformation rate. (**B**) Vertical deformation rate

direction were formed (Figs. 9; 12(O); and 16(B)). An obvious local collapse appeared along its lower boundary, and the collapse area expanded over time (Fig. 16(C, D, and E)). The deformation phenomena in zone IV are similar to those in zone III and display

Fig. 14 The boundary characteristics of upstream deformation zone III. **a, b** Local multistage scarps in zone III. **c, d** Characteristics of the upstream boundary. The locations of **a, c,** and **d** are listed in Fig. 9
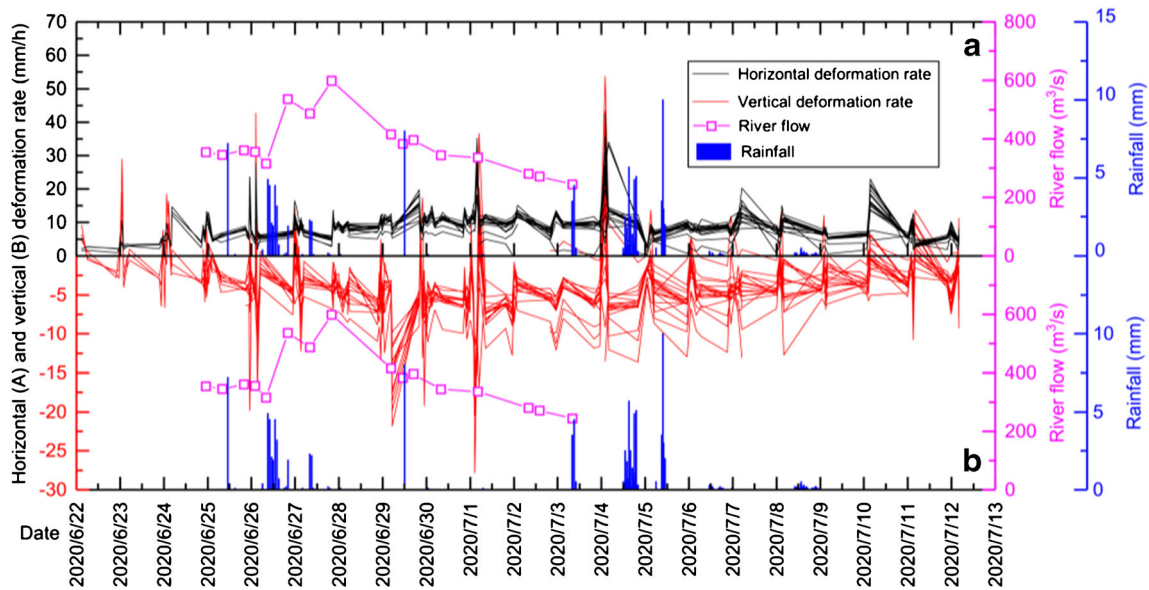
Fig. 15 The deformation rate of monitoring points in upstream deformation zone III. (**A**) Horizontal deformation rate. (**B**) Vertical deformation rate

approximately uniform deformation at present, as shown in Fig. 17; the current deformation rate is approximately 5 mm/h.

Discussion

To detect the current deformation state of the reactivated area, the landslide early warning system of creep slope failure, developed by SKLGP, is adopted (Fig. 18; Fan et al. 2019, Xu et al. 2020). According to this early warning system, the failure process of a landslide can be divided into 3 deformation phases: initial deformation, constant deformation, and accelerating deformation. In the first phase, the deposit produces an initial deformation, which often presents a parabolic distribution ($\triangle v < 0$). In the constant deformation stage, the slope enters a constant deformation state with a constant deformation rate ($\triangle v = 0$). Finally, the deposit deformation exhibits a sudden acceleration when it enters a highly accelerated state according to creep theory (Fan et al. 2019, Loew et al. 2016).

According to the results of emergency monitoring (Figs. 11, 13, 15, and 17), the reactivated area experienced an increase and decrease in the deformation rate, and an obvious parabolic distribution of deformation ($\triangle v < 0$) was formed. At present, the reactivated ANZ landslide
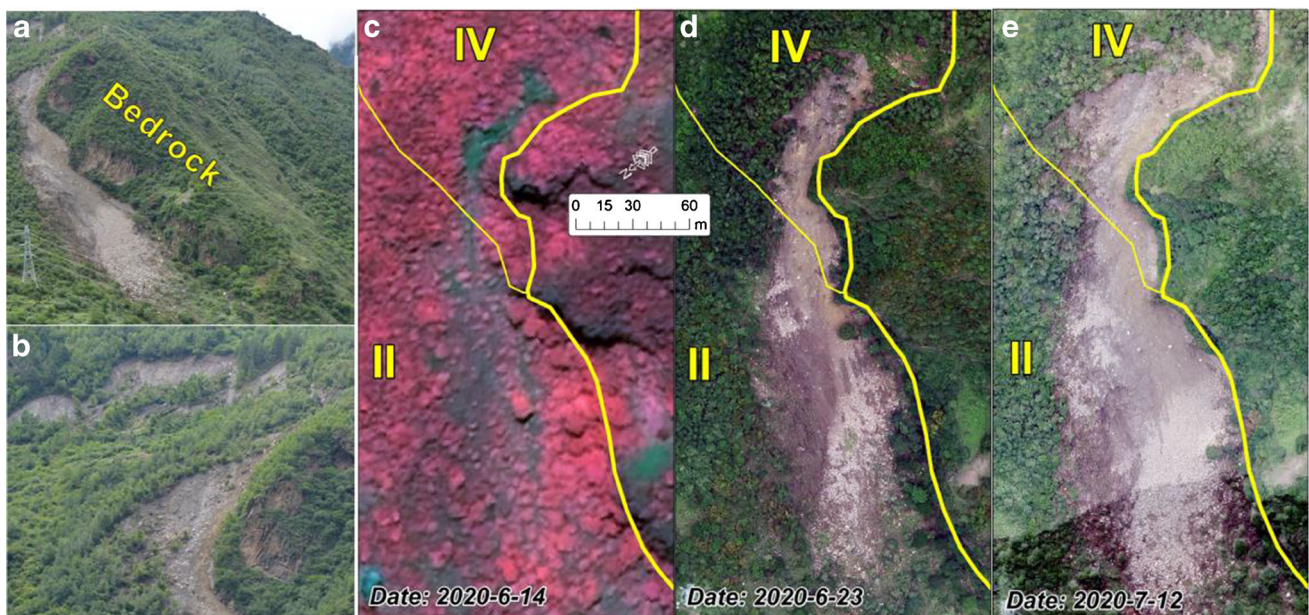

Fig. 16 The field images show the outcrop of bedrock (**A**) and the local head scarp (**B**), and the satellite and UAV images show the evolution process of the local collapse on different dates (**C**, **D**, **E**). Image (**B**) is from Gaofen-2. The locations of (**A**), (**B**), and (**C**) are listed in Fig. 9
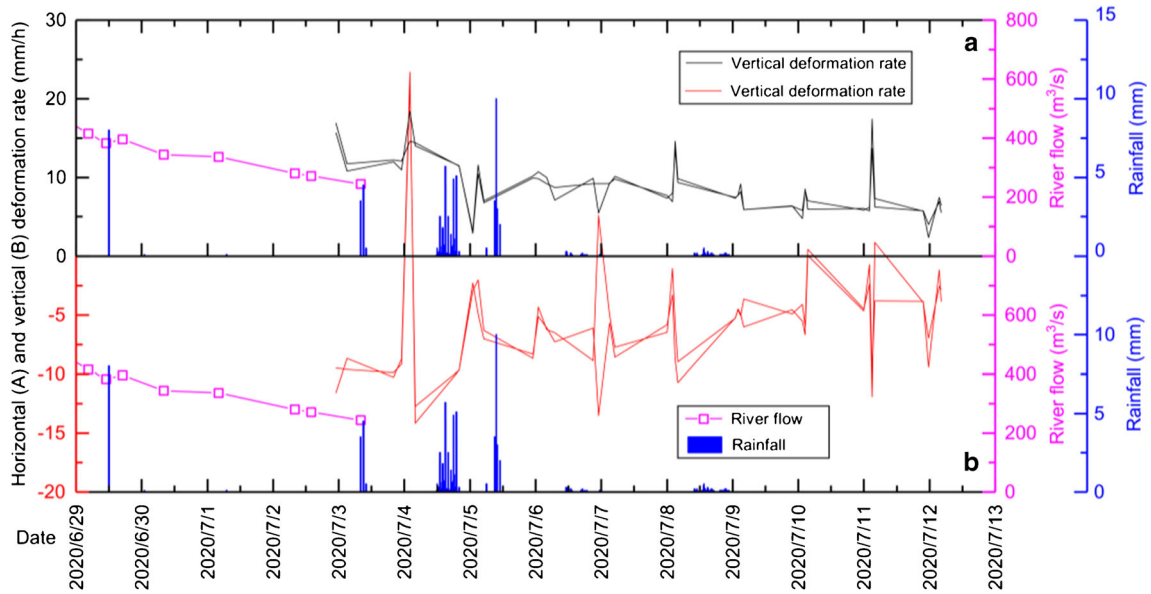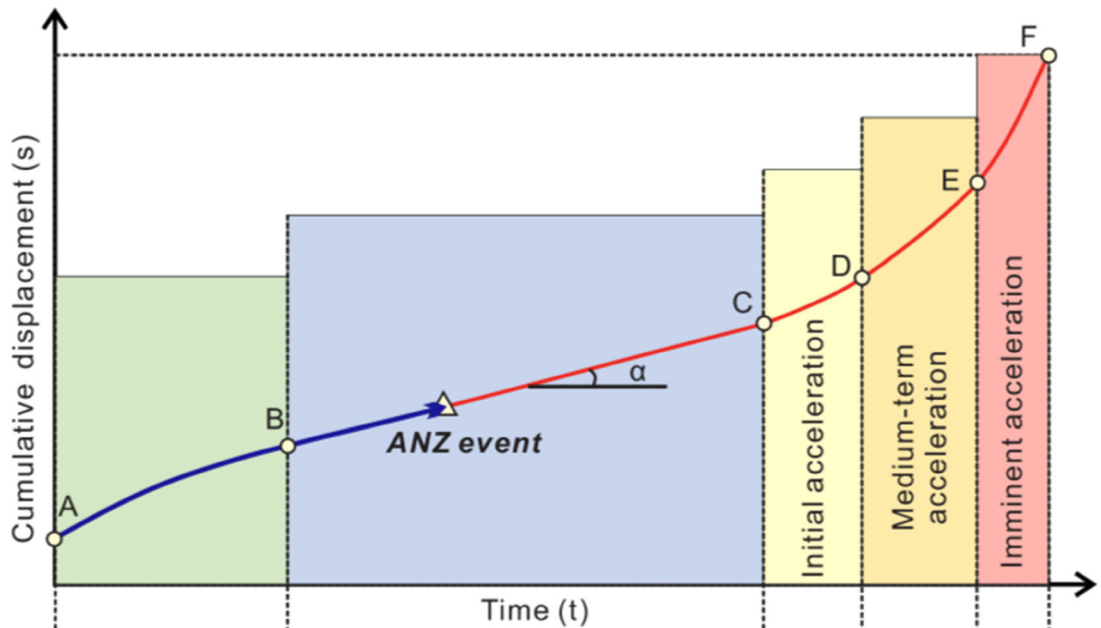
Fig. 17 The deformation rate of monitoring points in downstream deformation zone IV. (**A**) Horizontal deformation rate. (**B**) Vertical deformation rate

Fig. 18 The warning criteria of the landslide early warning system and the potential current state of the reactivated ANZ landslide. V_1—attention deformation rate, V_2—caution deformation rate, V_3—vigilance deformation rate, the detailed information of this early warning system is listed in Fan et al. (2019) and Xu et al. (2020)

maintains a consistent deformation rate (approximately 5 mm/h, $\triangle v = 0$), which indicates that the ancient ANZ landslide is in the constant deformation state (Fig. 18). The constant deformation state requires special attention, as indicated by the early warning system, and some emergency measures should be taken into consideration to prevent it from entering the next phase with catastrophic consequences.

Conclusion

On the night of June 16, 2020, an unexpected short-duration rainstorm with a cumulative rainfall of 38.1–42.4 mm struck the Meilong valley and triggered the Meilong debris flow. The debris flow, whose volume was approximately 4×10^5 m³, raised the riverbed by 8–12 m, and the backwater formed a dammed lake. Then, the river overflowed the front section of the deposit and formed a new river channel at the foot of the ancient ANZ landslide. The intense erosion caused the front section to collapse abruptly and reactivated the ancient ANZ landslide.

The reactivated ANZ landslide is sliding downward as a whole, and it covers an area of 0.62 km² and can be divided into 4 subzones: zone I—front collapse zone; zone II—main deformation zone; zone III—upstream deformation zone; and zone IV—downstream deformation zone. The deformation rates of zone I and II presented gradual decreases over time and remained at approximately 5 mm/h until July 12, 2020. The deformation rates of zone III and IV presented initial increases followed by decreases and remained at approximately 5 mm/h on July 12, 2020. At present, the reactivated landslide is in a constant deformation state.

References

Bai YJ, Wang YS, Ge H, Tie YB (2020) Slope structures and formation of rock–soil aggregate landslides in deeply incised valleys. J Mt Sci 17(2):316–328

Barla G, Debernardi D, Perino A (2015) Lessons learned from deep-seated landslides activated by tunnel excavation. Geomech Tunnelling 8(5):394–401

Borgatti L, Corsini A, Barbieri M, Sartini G, Truffelli G, Caputo G, Puglisi C (2006) Large reactivated landslides in weak rock masses: a case study from the Northern Apennines (Italy). Landslides 3(2):115–124

Bozzano F, Esposito C, Martini G, Martino S, Prestininzi A, Rinaldis D, Mugnozza GS (2013) Earthquake-reactivated landslide scenarios in Southern Italy based on spectral-matching input analysis. B Earthq Eng 11(6):1927–1948

Burda J, Hartvich F, Valenta J, Smítka V, Rybár J (2013) Climate-induced landslide reactivation at the edge of the Most Basin (Czech Republic)-progress towards better landslide prediction. Nat Hazards Earth Syst Sci 13(2):361–374

CIGMR (1985a) Geological map of Xiaojin County (1:20w). Map No. H-48-VII. (In Chinese)

CIGMR (1985b) Geological map of Danba County (1:20w). Map No. H-47-XII. (In Chinese)

Dai F, Lee C, Deng J, Tham L (2005) The 1786 earthquake-triggered landslide dam and subsequent dam-break flood on the Dadu River, southwestern China. Geomorphology 73(3):277–278

Dixon N, Spriggs MP, Smith A, Meldrum P, Haslam E (2015) Quantification of reactivated landslide behaviour using acoustic emission monitoring. Landslides 12(3):549–560

Fan X, Xu Q, Liu J, Subramanian SS, Zhou L (2019) Successful early warning and emergency response of a disastrous rockslide in Guizhou Province, China. Landslides 16(12):2445–2457

Flageollet JC, Maquaire O, Martin B, Weber D (1999) Landslides and climatic conditions in the Barcelonnette and Vars basins (Southern French Alps, France). Geomorphology 30(1–2):65–78

Gu DM, Huang D, Yang WD, Zhu JL, Fu GY (2017) Understanding the triggering mechanism and possible kinematic evolution of a reactivated landslide in the Three Gorges Reservoir. Landslides 14(6):2073–2087

Hewitt K (1988) Catastrophic landslide deposits in the Karakoram Himalaya. Science 242:64–67

Huang RQ (2009) Some catastrophic landslides since the twentieth century in the southwest of China. Landslides 6(1):69–81

Keefer DK (1994) The importance of earthquake-induced landslides to long-term slope erosion and slope-failure hazards in seismically active regions. Geomorphology 10:265–284

Korup O, Clague JJ, Hermanns RL, Hewitt K, Strom AL, Weidinger JT (2007) Giant landslides, topography, and erosion. Earth Planet Sci Lett 261:578–589

Li W, Zhao B, Xu Q, Yang F, Fu H, Dai C, Wu XX (2020) Deformation characteristics and failure mechanism of a reactivated landslide in Leidashi, Sichuan, China, on August 6, 2019: an emergency investigation report. Landslides 17:1405–1413

Li J (2012) Risk assessment of geological hazard after earthquake in Xiaojin County. Chengdu University of Technology M.D. Thesis. (In Chinese with English Abstract)

Lin GW, Chen H, Petley DN, Horng MJ, Wu SJ, Chuang B (2011) Impact of rainstorm-triggered landslides on high turbidity in a mountain reservoir. Eng Geol 117(1–2):97–103

Loew S, Gschwind S, Gischig V, Keller-Signer A, Valenti G (2016) Monitoring and early warning of the 2012 preonzo catastrophic rockslope failure. Landslides 14:141–154

Luo G, Hu X, Bowman ET, Liang J (2017) Stability evaluation and prediction of the Dongla reactivated ancient landslide as well as emergency mitigation for the Dongla Bridge. Landslides 14(4):1403–1418

Massey CI, Petley DN, McSaveney MJ (2013) Patterns of movement in reactivated landslides. Eng Geol 159:1–19

Matsuura S, Asano S, Okamoto T (2008) Relationship between rain and/or meltwater, pore-water pressure and displacement of a reactivated landslide. Eng Geol 101(1–2):49–59

Paronuzzi P, Bolla A (2012) The prehistoric Vajont rockslide: an updated geological model. Geomorphology 169:165–191

Prior DB, Suhayda JN, Lu NZ, Bornhold BD, Keller GH, Wiseman WJ, Yang ZS (1989) Storm wave reactivation of a submarine landslide. Nature 341(6237):47–50

Song K, Wang F, Yi QLS (2018) Landslide deformation behavior influenced by water level fluctuations of the Three Gorges Reservoir (China). Eng Geol 247:58–68

Su LJ, Hu KH, Zhang WF, Wang J, Lei Y, Zhang CL, Zheng QH (2017) Characteristics and triggering mechanism of Xinmo landslide on 24 June 2017 in Sichuan, China. J Mt Sci 14(9):1689–1700

Wang F, Zhang Y, Huo Z, Peng X, Wang S, Yamasaki S (2008) Mechanism for the rapid motion of the Qianjiangping landslide during reactivation by the first impoundment of the Three Gorges Dam reservoir, China. Landslides 5(4):379–386

Wang Y, Zhao B, Li J (2018) Mechanism of the catastrophic June 2017 landslide at Xinmo village, Songping river, Sichuan province, China. Landslides 15(2):333–345

Xu Q, Pei XJ, Huang RQ (2009) Large-scale landslides induced by Wenchuan earthquake. Science press, Beijing Book: In Chinese

Xu Q, Peng DL, Zhang S, Zhu X, He CY, Qi X, Zhao KY, Xiu DH, Ju NP (2020) Successful implementations of a real-time and intelligent early warning system for loess landslides on the Heifangtai terrace, China. Eng Geol 278:1–20

Zhao B (2020) The mechanism of large earthquake-triggered landslides in area of high intensity and deep canyon of Northwest Sichuan. Chengdu University of Technology. Ph.D thesis. (In Chinese with English Abstract)

Zhao B, Li W, Wang Y, Lu J, Li X (2019) Landslides triggered by the Ms 6.9 Nyingchi earthquake, China (18 November 2017): analysis of the spatial distribution and occurrence factors. Landslides 16(4):765–776

B. Zhao · L. Su · L. Zeng
Key Laboratory of Mountain Hazards and Earth Surface Processes, Institute of Mountain Hazards and Environment,
Chinese Academy of Sciences,
Chengdu, 610041, China

H. Zhang (✉) · W. He · H. Qin
Sichuan Metallurgical Geological Survey and Design Group Co., Ltd,
Chengdu, 610081, China
Email: zhanghaiquan1210@163.com

L. Hongjian
School of Human Settlements and Civil Engineering,
Xian Jiaotong University,
Xi'an, 710049, China

W. Li
State Key Laboratory of Geohazard Prevention and Geoenvironment Protection,
Chengdu University of Technology,
Chengdu, 610059, China

L. Su
CAS Center for Excellence in Tibetan Plateau Earth Sciences,
Beijing, 100101, China

L. Su
China-Pakistan joint Research Center on Earth Sciences,
Islamabad, Pakistan

L. Su (✉)
University of Chinese Academy of Sciences,
Beijing, 100049, China
Email: sulijun1976@163.com

M. R. Dhital
Central Department of Geology,
Tribhuvan University,
Kathmandu, Nepal